SSRG International Journal of Mechanical Engineering
ISSN: 2348-8360/ https://doi.org/10.14445/23488360/IJME-V13I7P101

Volume 13 Issue 7, 1-15, July 2026

Original Article

Numerical and Statistical Investigation of Performance and Emission Parameters in a GDI Engine Equipped with Passive Pre Chamber

Karthikeyan M[1], Ramesh P[2], Edward James Gunasekaran[3]

[1,2,3]*Department of Mechanical Engineering, Annamalai University, Tamil Nadu, India.*

[1]*Corresponding Author : karthikbe9566@gmail.com*

Received: 09 April 2026 Revised: 10 June 2026 Accepted: 25 June 2026 Published: 30 July 2026

Abstract *- The increase in pollutant formation globally by the utilization of IC engines leads to the implementation of stringent norms worldwide. The aim of this work is to reduce emission formations and improve GDI engine efficiency with a Pre-Combustion Chamber (PCC) by finding optimal factors of statistical analysis using Response Surface Methodology (RSM). An SI engine having GDI equipped with a six-hole orifice PCC is optimized using RSM in the design of experiments. Key factors such as orifice throat angle, injection pressure, and L/D ratio were considered in RSM design, and responses were observed with Box-Behnken design techniques. Before conducting a CFD simulation for the statistical analysis method, validation of the CFD simulation was performed. The CFD setup designed for different runs of the statistical RSM approach and optimal factors of simulation predicts the accuracy of RSM responses and helps confirm optimal factors for engine operating conditions of a six-hole PCC in a GDI engine. Peak cylinder pressure achieved for the CFD-simulated model is 66.39 bar, indicating an error percentage of 1.94% higher than the RSM model. The percentage of error between the RSM and optimal factors of the simulation was less than 4% compared to the heat release rate and NOx.*

Keywords *- Computational Fluid Dynamics, Pre-Combustion Chamber, Response Surface Methodology, Spark ignition engine, CFD, GDI, PCC.*

1. Introduction

Over the past few decades, the quality of the ambient air has been declining, particularly in urban areas [1]. Vehicle emissions are an important factor contributing to the decrease in ambient air quality [2]. The automotive industry has focused on creating cleaner and more efficient internal combustion engines due to the increased environmental concerns and strict emission requirements, such as BS-VI and Euro criteria that have been implemented globally [3]. Traditional Spark Ignition (SI) engines, which were widely used, face challenges in meeting these new standards, particularly regarding NOx emissions [4]. Particulate matter generation is a disadvantage of gasoline direct injection, but it is a promising solution that increases power output and fuel efficiency [5]. TO minimize NO_x, the application of a pre-combustion chamber to a GDI engine is introduced, which helps in combustion stability and to burn ultra-lean mixtures, and CFD methodology provides a comprehensive analysis of the SI engine [6]. The Reynolds-Averaged Navier-Stokes (RANS) approach significantly reduces computational time by averaging the governing Navier-Stokes equations over time. This process models the effects of turbulence rather than resolving every fluctuating eddy, which are the smallest, most energy-consuming fluid motions [7]. Flame spatial distribution inside PCC directly correlates with combustion stability. Tangential hole design provides superior combustion stability compared to radial holes. Radial holes create significantly higher cycle-to-cycle dispersion in PCC flow [8]. Parameters such as air-fuel ratio, turbulence stratification and dynamic behavior of jets influence the flow fields while jets passing through the PCC orifice into the main cylinder [9]. Smaller nozzle diameters create more intense reacting jets and stronger gas choking conditions, influence flow field patterns, and enhance jet penetration and mixing characteristics [10]. The mixture's enleanment raised the velocity ratio, which caused the distributed regimes to shift the fractured reaction zone and considerably reduce the flame propagation speed in PCC [11, 12].

The geometry of PCC and engine operating parameters performs vital role in the performance of the engine [13, 14]. Related to the ordinary ignition system, the turbulent ignition system's combustion was more rapid and sophisticated. High-quality combustion results from the PCC system's extension of the air-fuel mixture's flammability limit [15, 16]. Heat losses in boundaries and phasing of combustion were significantly affected by flame jet velocity from PCC to the main chamber [17, 18]. The ignition delay time is decreased through the use of a PCC [19]. The L/D ratio of the orifice and diameter of throat impact jet characteristics and combustion performance, and also enhances flow at the orifice, leads to differences in pressure and jet velocity [20], [21]. Through the optimization of pre-chamber geometrical factors such as L/D ratio and orifice throat angle, we can be able to increase the engine efficiency [22].

The jet development and stability change happen due to the pressure differentials in the narrow throat PCC design [23, 24]. The percentage of NOx and CO emissions generated inside PCC itself rises during PCC volume is decreased. Pollutants may occur as a result of more intense combustion conditions inside smaller prechambers [25]. Compression ratio, injection pressure, and timing are important optimized factors that significantly increase brake thermal efficiency and lower emissions [26, 27]. Using the desirability approach, response surface methodology aids in optimizing emissions in response [28]. RSM approaches were used to optimize the combined impact of Start Of Injection (SOI) and Exhaust Gas Recirculation (EGR) on engine performance and emissions [29]. Numerous interconnected design elements, including pre-chamber volume, orifice number, and orifice diameter, affect the engine's combustion and emission characteristics in pre-chamber GDI engines. The Box-Behnken design helps in determining and measuring the factors' interaction effect [30, 31].

Pre-chamber ignition systems have been the subject of numerous research studies that have looked at their potential to increase combustion stability and lower emissions [32, 33], but little is known about how certain design and operating factors affect overall performance. Few studies have examined the individual impacts of orifice angle, injection pressure, and L/D ratio; most of the work that has been done so far has concentrated on individual components such as nozzle size, chamber volume, or overall geometry [34, 35]. In ultra-lean settings, steady ignition and effective combustion depend on these factors, which also have a direct impact on jet penetration, turbulence production, and mixture preparation. The above studies imply the individual methodology to analyze prechamber engines, while the significance of using RSM methodology is lacking, which helps to minimize computational cost and for effective engine optimization.

The goal is to investigate the critical design and operating parameters, such as PCC orifice L/D ratio, throat angle, and injection pressure. The hypothesis of this research work is to reduce computational effort through the integration of CFD with RSM, and also the geometrical influence of PCC on combustion and emission characteristics. The pre-combustion chamber is widely used for its lean-burn capability. However, optimization studies on its geometrical factors combined with statistical design methods are limited. The originality of the research work is in the use of the Box-Behnken design to optimize pre-combustion chamber geometrical parameters and also in the multi-response optimization approach. Several studies related to pre-chamber ignition systems have been done, but regarding the optimization of six-hole passive pre-chamber geometry and its influence on performance and emission parameters, it is not discussed, nor is the combined approach of CFD and statistical optimization explored. The uniqueness of this work relies on the CFD-based investigation of a six-hole passive pre-chamber, optimization of multiple responses, statistical evaluation of RSM, and identification of optimum pre-chamber parameters.

2. Materials and Methods

A simulation approach is performed to analyze internal combustion engine performance and emission characteristics. The modelling process was conducted step by step with the use of the required geometrical data. The prepared geometrical model is diagnosed for surface errors such as intersections, open edges, and non-manifold errors. Boundaries were separated using different color identification, and ID numbers were assigned. The case setup was prepared, and it was mandatory to assign boundary conditions such as velocity, temperature, and pressure. A crank angle-based simulation approach is carried out; engine details, valve timings, simulation time parameters and injection parameters are given as shown in Table 1. Fuel properties and fuel injection parameters, such as the fuel reaction mechanism with oxygen at particular temperatures and pressures inside the cylinder and the location of the nozzle and injector, injector diameter, and spray cone angle length and diameter, were given. The injector model has a 10-degree spray cone angle and a 0.0003-meter nozzle diameter. Smaller nozzle diameters help to achieve improved atomization of fuel and reduced emissions [36]. Initialization settings such as cylinder temperature, species found, and fraction of species were determined. Solver settings consist of PISO (Pressure-Implicit with splitting of operators) solver chosen to solve Navier-Stokes equations due to its accuracy for compressible flows and reduced iterations per time step [37].

Inside the cylinder, the turbulent flow is highly unsteady and consists of strong swirl, squish, and jet interactions while combustion takes place. So in order to capture these turbulent variations, the Reynolds-Averaged Navier-Stokes equations approach is adopted with the RNG k-epsilon turbulence model, and also, while compared with standard K-epsilon, RNG k-epsilon provides improved stability with less computational cost. The modeling of combustion was conducted by the selection of the SAGE combustion model because of its ability to solve detailed chemical kinetics, which leads to better prediction of flame propagation. The prediction of fuel behavior when injected is very vital for better predictions. The Kelvin-Helmholtz Rayleigh-Taylor spray breakup model is used to solve high-pressure injections and to predict droplet breakup. Boundary conditions were applied according to the engine operating conditions. Boundaries were separated individually, such as the piston, liner, pre-chamber, head, and valves. A piston is a moving boundary, so translating motion is applied with temperature with respect to the operating conditions. Valve profiles were given for translating valves, while other boundaries were static boundaries. The convergence criteria were adopted to ensure numerical stability by monitoring the residuals of governing equations at each time step, i.e., simulations were considered converged when residuals were reduced below 0.0001 to 0.000001.

Table 1. Engine specifications, valve timing and injection parameters

Parameter	Specifications
Bore	86mm
Stroke	86mm
Displacement	499.5cm^3
Speed	1000rpm
Compression Ratio	9.2
Connecting rod length	145mm
Simulation Period	720^{O}CA
Inlet Valve Opening	10^{O}bTDC (Before
Inlet Valve Closing	55^{O}aBDC (During
Exhaust Valve Opening	55^{O}aBDC (During
Exhaust Valve Closing	10^{O}aTDC (During
Start of Injection (SOI)	-370.0^{O} CA
Injection Duration(50, 100 and 150 Bar)	55.907^{O} CA
Fuel Type	Gasoline

Figure 1 displays a front view of the engine with case setup and a magnified view of the pre-chamber attached to the engine cylinder. The PCC consists of six orifices that connect the cylinder region. Parameters such as orifice diameter, angle along the pre-chamber axis, and L/D ratio are important for optimizing flame travel into the main combustion chamber [38]. Improper designs will lead to poor combustion in the PCC, which leads to poor combustion in the main cylinder. These factors will directly influence the performance and emission parameters, respectively. Density-based solvers that improve solution stability were selected because of the high-speed flames traveling through orifices from the PCC to the main chamber; rapid pressure and density changes occur inside the cylinder. Energy equations can be solved in a fully coupled manner using this type of solver, and there is better handling of species transport in multiphase combustion scenarios.

The boundary conditions given were based on operating conditions of the engine, such as pressure, wall temperatures, inflow and outflow boundaries, and static and moving boundaries. No slip wall boundary conditions were given for solid surfaces. A fixed embedding meshing strategy was implemented along with the base grid for the critical regions, such as intake and exhaust valve angles, spark plug region, and throughout the cylinder, to obtain better numerical results.

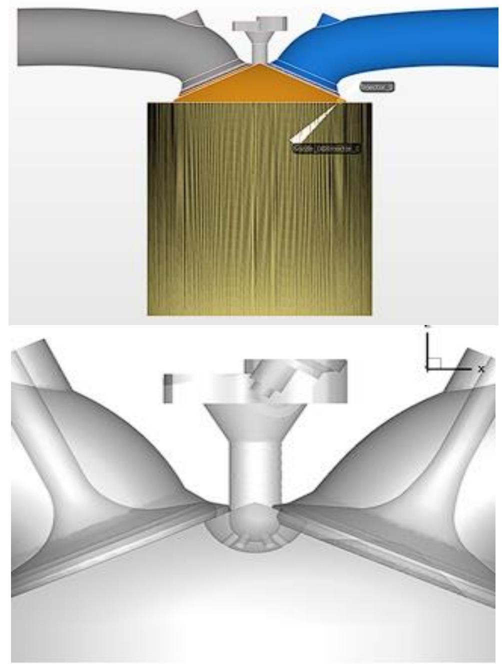

Fig. 1 Schematic front and magnified view of pre chamber attached with cylinder

Accurate prediction of turbulence is particularly crucial in combustion modeling since it directly affects flame kernel development, burn rate, and emissions [39]. A mesh independence study is held to validate the CFD model, as shown in Figure 2. Experimental data and CFD simulations consisting of 4 mm, 6 mm, 8 mm, and 10 mm varying grid sizes were plotted. The x-axis, which shows the crank angle from -360 ° CA to 0 ° CA, and the y-axis shows the instantaneous fluctuation velocity along the cylinder's z-axis region. Observation of the plot shows that the 4 mm grid size has the best agreement with experimental data compared with other grid sizes. When compared to experimental data, the divergence increases with coarser grid sizes. Compared to the 4 mm grid size, grid sizes of 6 mm, 8 mm, and 10 mm exhibit a sharp drop in turbulence around -260^{0}CA after the turbulence peak is reached.

The 4mm grid size improved the resolution of parameters such as scale eddies and flow gradients. Also, the size of the grid was validated through consideration of 4mm, 6mm, 8mm, and 10mm. This is also known as the study of grid independence. So from this validation, the grid size 4mm confirmed better results and followed the trends of experimental data very closely. This study was conducted before coined the number of runs of simulation through the Box-Behnken design method in RSM. Once the optimal factors and response were obtained, the validation of the optimal simulation from the optimal factors in RSM with the CFD simulation response. Both the RSM optimal response and CFD optimal factors of simulation were confirmed by the very low % of error, and this was also discussed in the results.

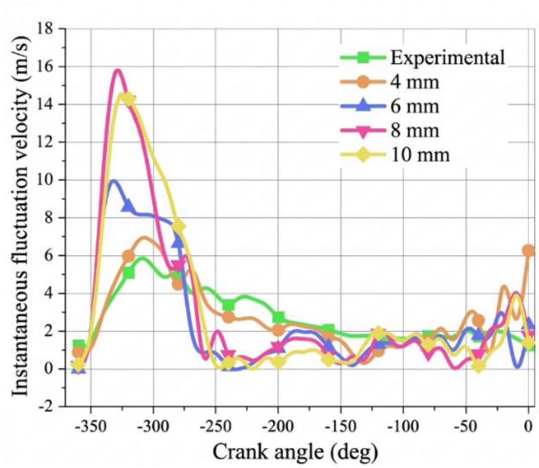

Fig. 2 Mesh independence study

Response Surface Methodology (RSM) uses the statistical technique of Box-Behnken Design (BBD) to improve processes that are affected by a number of variables [40]. It is also helpful for creating second-order (quadratic) models without needing a complete factorial design, which lowers computational costs and improves the viability of simulations and experiments [41]. BBD arranges the points of experiments at the midpoints of the edges of the experimental domain includes several centre points to estimate experimental error [42]. For a three-factor design, BBD requires a number of design points, such as 17 runs, which consists of 5 centre points, i.e., repeatable experiments [43]. The name and the number of factors and their low-level values and high-level values were given as shown in Table 2. Table 3 displays the coded factor levels for a Box-Behnken design with six responses. N=2K (K-1) + Co, where k is the number of factors and Co is the number of central points, is the formula needed to develop BBD [44].

Table 2. Input factors and their ranges used in the Box-Behnken design

Factors	Description	Low Level	High Level
A	Throat Angle(deg)	45	70
B	Injection Pressure (bar)	50	150
C	L/D ratio	1	2

Table 3. Coded factor levels and six responses

Run	Surface			Normalized Response					
	Orifice Throat –A Angle (deg)	Injection Pressure –B (Bar)	L/D Ratio-C	Pressure (%)	Temperature (%)	HRR (%)	CO (%)	CO_2 (%)	NO_x (%)
1	45	50	1.5	63.918	2671.92	173.556	39.329	58.1054	0.183022
2	57.5	100	1.5	64.912	2637.07	207.901	43.9599	54.4718	0.138366
3	70	100	2	65.037	2646.05	259.262	43.3589	54.8888	0.0660032
4	57.5	100	1.5	64.912	2637.07	207.901	43.9599	54.4718	0.138366
5	70	150	1.5	64.656	2690.48	215.57	38.1914	58.4628	0.194615
6	45	150	1.5	62.672	2670.65	211.661	37.9283	58.7505	0.101471
7	70	50	1.5	64.15	2654.16	241.106	41.2783	56.6636	0.173627
8	70	100	1	64.342	2642.67	240.868	43.7008	54.6514	0.0642853
9	57.5	50	2	66.054	2673.51	188.649	40.0404	57.5696	0.175095
10	57.5	150	2	65.046	2681.2	223.259	38.2129	58.5484	0.0947269
11	45	100	2	63.737	2630.94	201.204	44.8034	53.8609	0.0560774
12	57.5	100	1.5	64.912	2637.07	207.901	43.9599	54.4718	0.138366
13	57.5	50	1	65.591	2669.97	197.549	41.6078	56.4375	0.069029
14	57.5	100	1.5	64.912	2637.07	207.901	43.9599	54.4718	0.138366
15	57.5	150	1	63.568	2664.04	229.057	40.3749	56.9242	0.169177
16	45	100	1	62.114	2647.02	224.193	41.6439	56.156	0.0717324
17	57.5	100	1.5	64.912	2637.07	207.901	43.9599	54.4718	0.138366

3. Results and Discussion

The Simulation work is conducted for 17 runs, and the response values were given. Furthermore, analysis of six responses was conducted individually, and no transformations were given for all six responses while forming the regression model, i.e., λ=1 for all responses, as monitored from the box-cox plots λ values lie within the confidence interval for responses pressure, temperature, CO and CO_2. However, for NO_x and heat release rate, it shows a curvature, which means that the optimal lambda is slightly less than one but within the range, as shown in Figure 3.

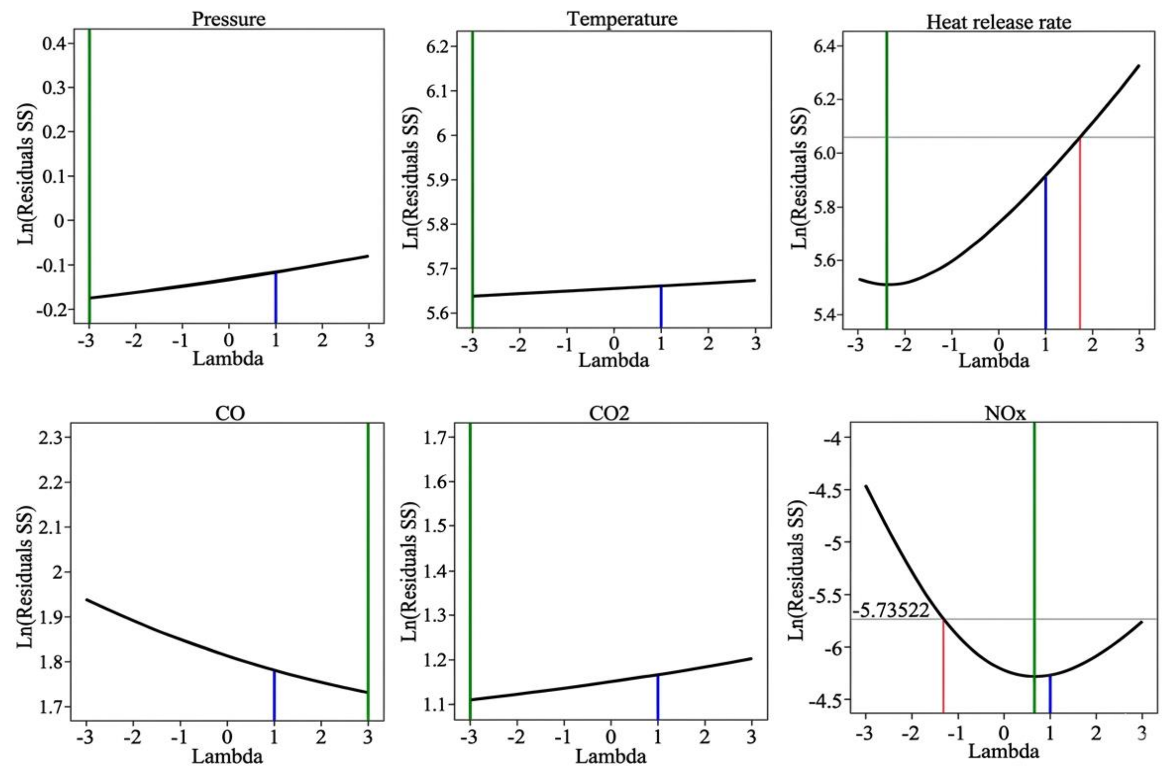

Fig. 3 Box-Cox plot for six responses

Table 4. ANOVA table

Response Variable	Sum of Squares (SS)	Degrees of Freedom (DF)	Mean Square	Model F-value	Model p-value	Model Significance
Pressure (bar)	15.08	9	1.68	13.19	0.0013	Significant
Temperature (K)	5317.54	9	590.84	14.39	0.0010	Significant
Heat release rate	6452.48	9	716.94	13.47	0.0012	Significant
CO (mg)	84.90	9	9.43	11.13	0.0022	Significant
CO_2 (mg)	44.51	9	4.95	10.78	0.0024	Significant
NO_x (mg)	0.0334	9	0.0037	13.73	0.0011	Significant

The quadratic process is selected to analyze the interaction and quadratic effects. Where interaction shows the combination of factor terms that influence the response, and quadratic terms capture the non-linear effects, which collectively gives us the regression model. Table 4 shows the sum of squares, model F-values and P-values for responses at a confidence level of 0.05 (95%), which represents that the overall model significance is good. Factors were considered as A, B, and C, where A is the throat angle, B represents the injection pressure, and C is the L/D ratio. The quadratic regression equation formed is given below in equation 1. The regression equation consists of constants, linear effects of factors, interaction between the factors, and the quadratic effects of the factors.

$$Y = \beta_0 + \beta_1 A + \beta_2 B + \beta_3 C + \beta_{12} AB + \beta_{13} AC + \beta_{23} BC + \beta_{11} X_1^2 + \beta_{22} X_2^2 + \beta_{33} X_3^2 \quad (1)$$

Table 5. Coefficient of determination for responses

Responses	R^2	Adjusted R^2	Predicted R^2	Adequate Precision
Pressure	0.9443	0.8728	0.1094	13.1459
Temperature	0.9487	0.8828	0.1796	10.4195
Heat release rate	0.9454	0.8752	0.1267	16.2887
CO	0.9347	0.8507	-0.0450	9.2759
CO_2	0.9327	0.8461	-0.0771	8.8607
NO_x	0.9464	0.8774	0.1419	11.3324

The coefficient of determination R^2 values are greater than 0.93, which shows 93% of the variability for the developed regression models as shown in Table 5. This clearly indicates that quadratic models provide a better relationship between the input factors and responses. Adjusted R^2 values range from 0.8461 to 0.8828, which is nearby to the corresponding R^2 values, and it indicates that no unnecessary terms affects regression equations. The adequate precision values for all responses are greater than 4, which indicates that the developed models are adequate for exploring the design space. When the model of each responses show the significance through the ANOVA table, which means the lack of fit test is insignificance. This indicates that regression models are suitable for the analysis of responses.

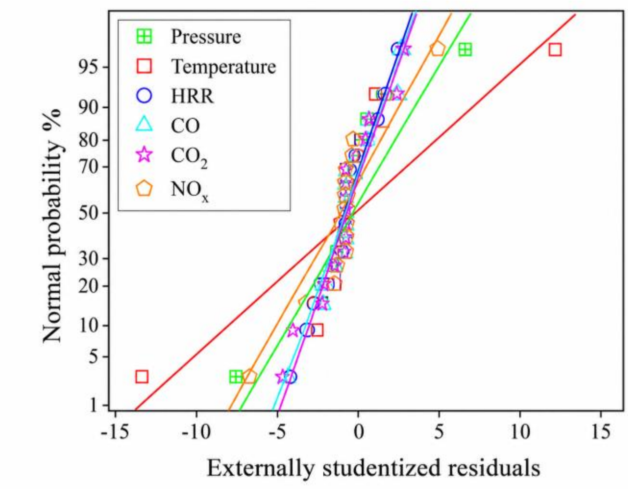

Fig. 4 Normal probability plot for the responses

The leftovers from the regression model were normally spread out. So we looked at a graph called a normal probability plot, which is shown in Figure 4. This graph has Z-scores on the bottom. The normal probability plot helps us understand how the regression model leftovers are distributed. We used the regression model leftovers to make this plot. The regression model leftovers are important to check. These scores were calculated from ranking the residuals. The vertical scale shows the residuals from the simulations. If the data were perfectly normal, all points would line up on a diagonal line. The values in this plot are close to the line. This closeness gives us confidence in the model's assumptions about the data and residuals. A couple of points, most noticeably those with residuals near ±7.917 sat well away from the rest, hinting at possible outliers. Although they stand apart, these few extremes did not affect the overall pattern, and the bulk of the points still followed the line closely enough to support the model's use within the tested range.

Cook's Distance was shown in Figure 5 to spot any runs that might be pulling the regression model more than the rest. Along the bottom of the plot are the run numbers, and the vertical scale shows the D_i values for each response. A horizontal red line marks the usual cut-off at D_i=1, above which a run can be considered influential. Most of the points sit well below this line, which means they have little sway over the fitted equations. Even so, a few cases, most notably runs 6, 7, and 8 in certain responses, rise above the boundary. These are the runs where a combination of higher leverage and larger residuals makes them stand out from the bulk of the data. That doesn't automatically mean they are wrong, but they simply reflect operating conditions that differ from the rest of the test space. Removing them would likely shift the model parameters, so they were kept, but with their influence noted. Overall, the low Cook's Distance for the majority of runs supports the stability of the models across the experimental domain.

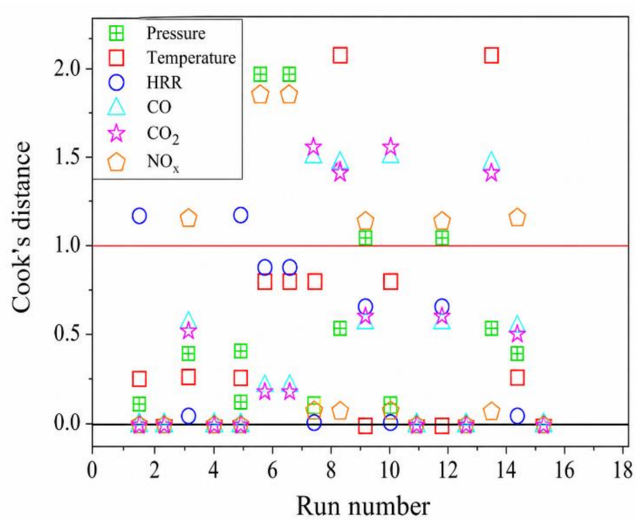

Fig. 5 Cook's distance values for identifying influential runs across responses

The residual patterns for pressure, temperature, Heat Release Rate (HRR), CO, CO_2, and NO_x were checked using externally studentized residual plots as shown in Figure 6. In each case, predicted values are on the axis. The vertical axis shows the residuals. There are lines that mark the plus or minus 4.81963 limits. Ideally, the points should not follow a clear pattern, and they should also stay within these limits. For pressure, CO, and CO_2, this was mostly the case, with residuals lying close to zero and no signs of systematic drift. As shown in Figure 6 for temperature, heat release rate and NO_x, one or two points or runs were found outside the boundary line, which indicates the outliers. Most of the data points for every response remained near the Z-score line and in the expected range, while some points deviated, and this doesn't influence the regression model.

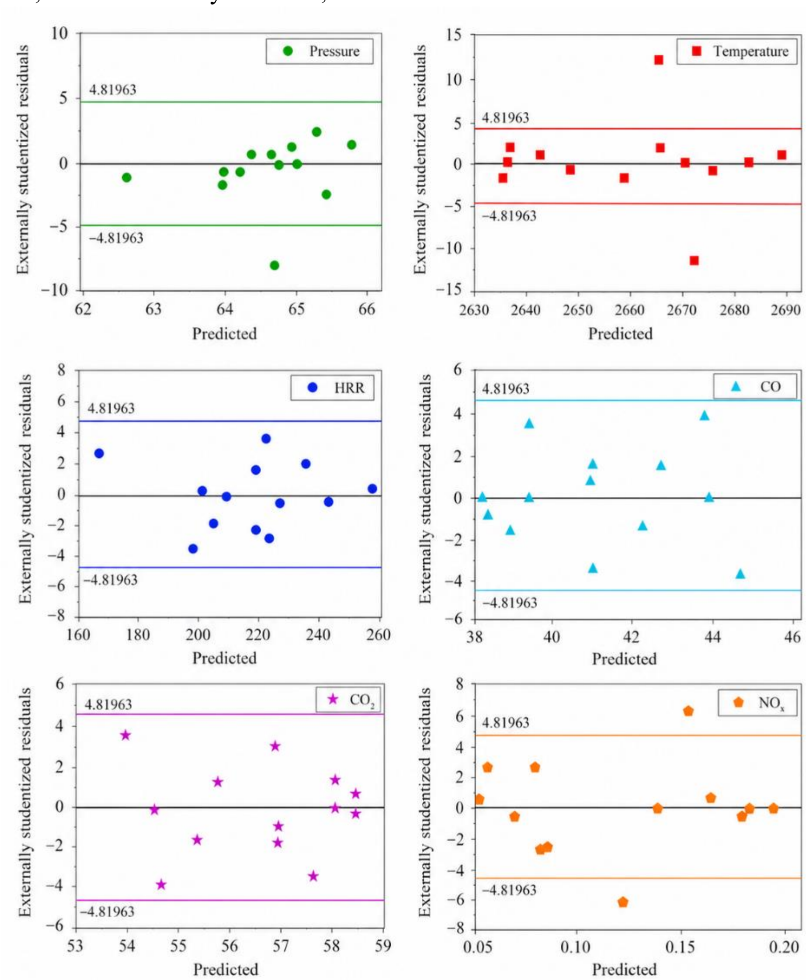

Fig. 6 Predicted Vs. externally studentized residuals for identification of outliers

The Figure 7 and 8 shows interaction effects of two factors, A and B, throat angle and injection pressure, while keeping C constant, i.e., the L/D ratio, on response pressure. Curvature on the surface plot and contour plot indicates that factors are not independent, which shows interaction effects on response, and the combination of factors throat angle and injection pressure contributes to the pressure variation.

The combination or interaction effect of factors A and B on response temperature is observed. Maximum values of throat angle and injection pressure lead to increased temperature predictions. Design points indicate the variation between the actual data and model prediction, either greater or lesser values.

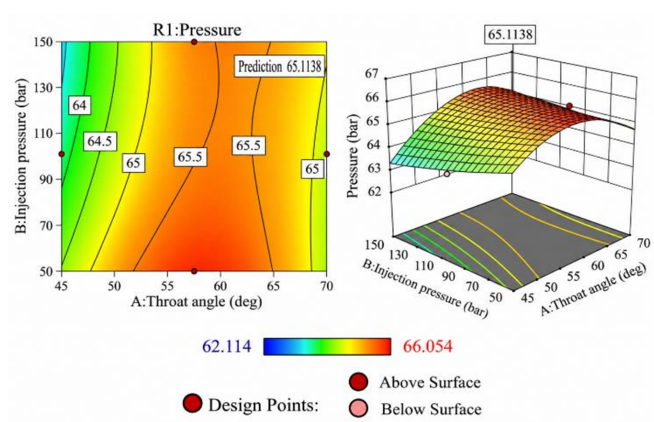

Fig. 7 2D contour and 3D surface plots of predicted response-pressure

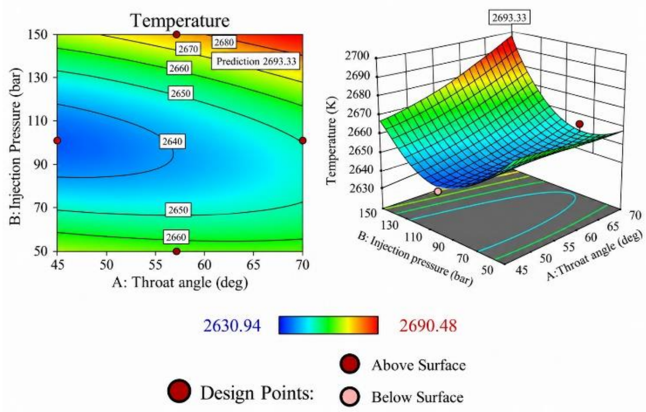

Fig. 8 2D contour and 3D surface plots of predicted response-temperature

A contour plot and a three-dimensional response surface, as shown in Figure 9, illustrate how the Heat Release Rate (HRR) is affected because the combination of injection pressure and throat angle. The contour plot's colourful areas, which range in value from roughly 174 J to 259 J, show variations in HRR. It is simpler to notice how the reaction changes over the factor space by using the contour lines, which are labelled with distinct HRR levels. The design points are highlighted with red markers indicates that the observed HRR was slightly higher than the model prediction, while lighter ones show the opposite. An increase in throat angle enhances HRR, and this effect becomes stronger when combined with higher injection pressure. The surface, however, does not rise uniformly; instead, it shows a curved profile, meaning the relationship is nonlinear. This curvature suggests that HRR increases up to a certain range of factor settings before the rate of improvement slows, pointing toward the existence of an optimum region. The model predicts a maximum HRR of 244.426 J, which is in good agreement with the surrounding design points. Finally, the combination of both factors, throat angle and injection pressure, strongly affects HRR, and the fitted model is able to capture their combined influence.

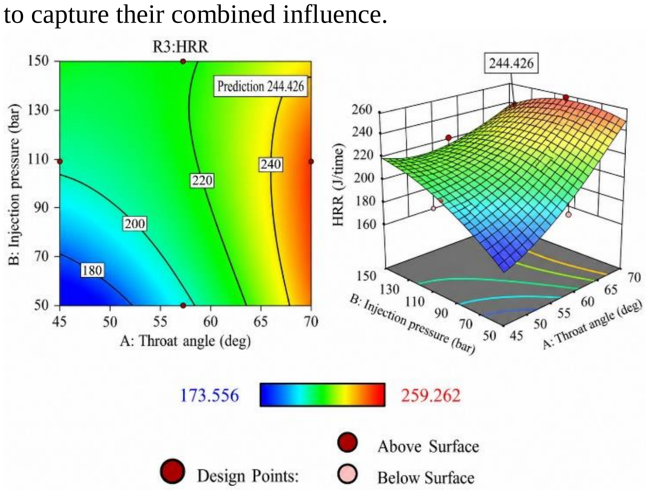

Fig. 9 2D contour and 3D surface plots of predicted response-HRR

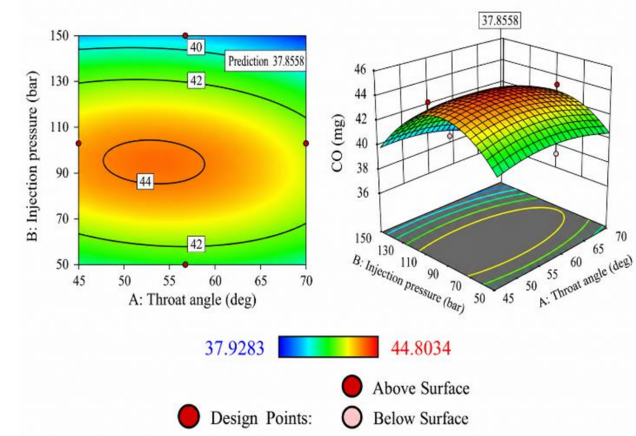

Fig. 10 2D contour and 3D surface plots of predicted response-CO

The interaction effect of throat angle and injection pressure on CO emission is shown in Figure 10. Results indicate a non-linear distribution, with values ranging from 37.93 mg to 44.8 mg. The surface plot shows the curvature of the response, which means quadratic behavior, while the design points match closely with the fitted surface.

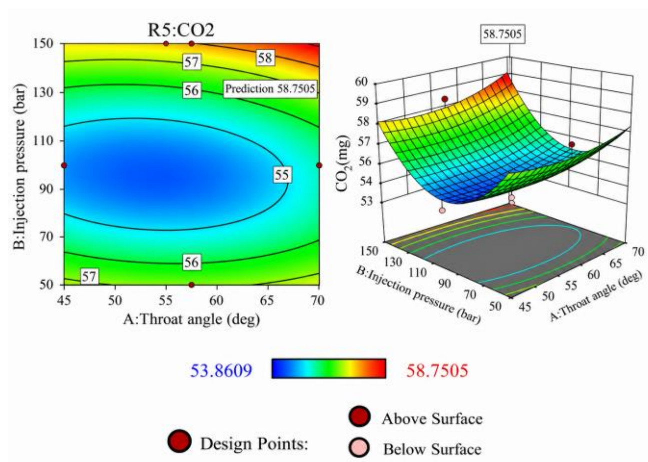

Fig. 11 2D contour and 3D surface plots of predicted response-CO_2

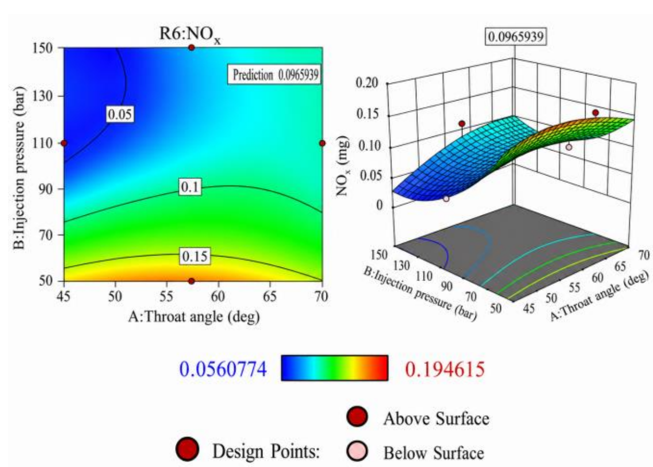

Fig. 12 2D contour and 3D surface plots of predicted response-NO_X

Figures 11 and 12 show how the injection pressure and throat angle affect CO2 and NOx emissions. The CO2 graphs clearly show that the response is not in a straight trend but formed as a curved pattern. A low-emission zone is created in the middle of the design space when the CO2 level falls at moderate injection pressures and neck angles. This suggests that the combustion process is more efficient and emits less CO2 when conditions are balanced. Nevertheless, as the injection pressure and neck angle are pushed toward higher values, the emissions rise once more; the maximum anticipated concentration is approximately 58.75 mg. As is common with quadratic effects, improvements are only apparent within a limited working window. However, a different story is told in the NOx plots. Here, the surface shows that NOx emissions tend to grow gradually with throat angle but tend to decrease with increasing injection pressure. Despite the relatively small magnitude of NOx, which ranges from roughly 0.056 to 0.195 mg, the graphs' curvature shows that the interaction between the two components has a significant impact on the reaction. At the centre of the space, the model shows a value of around 0.096 mg. This makes sense because when you increase the pressure of the fuel, it gets broken down into bits, which helps to keep the temperature from getting too high and produces less NOx. On the hand, if you make the throat angle bigger, it helps the air and fuel mix together better, which can make the flames hotter and actually creates more NOx. The model is talking about the space and the amount of NOx in the space, and how the model forecasts the amount of NOx in the space.

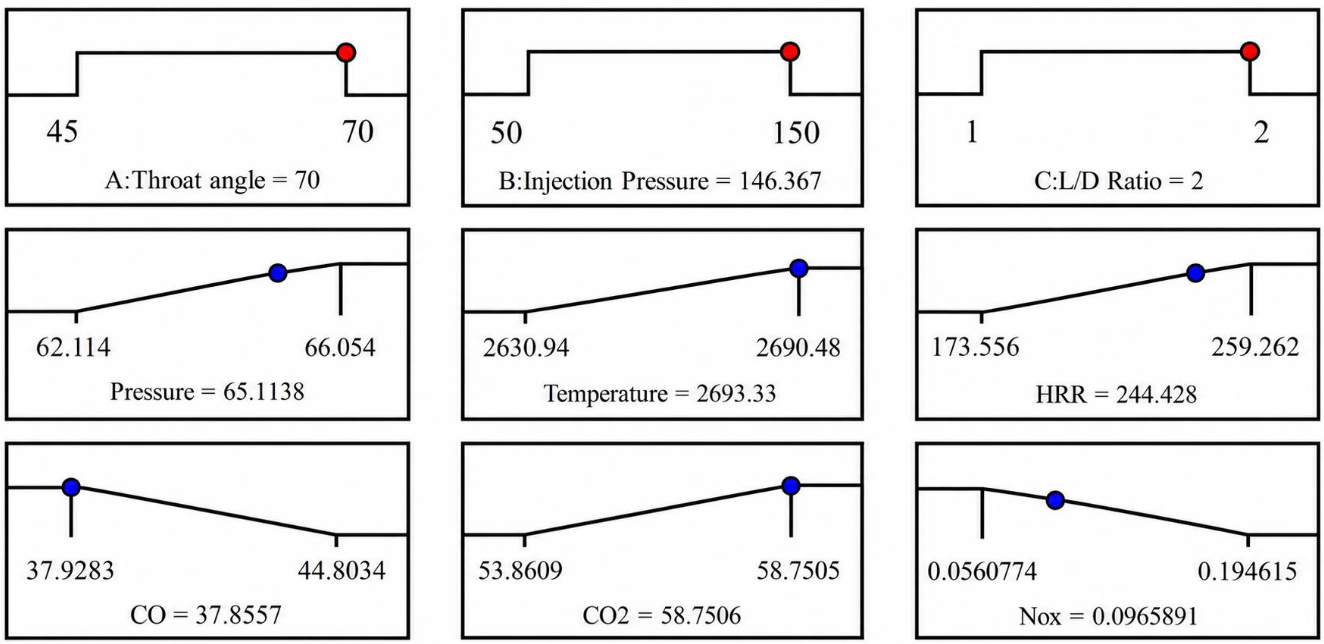

Fig. 13 Ramp plots indicate the optimized values for factors and responses

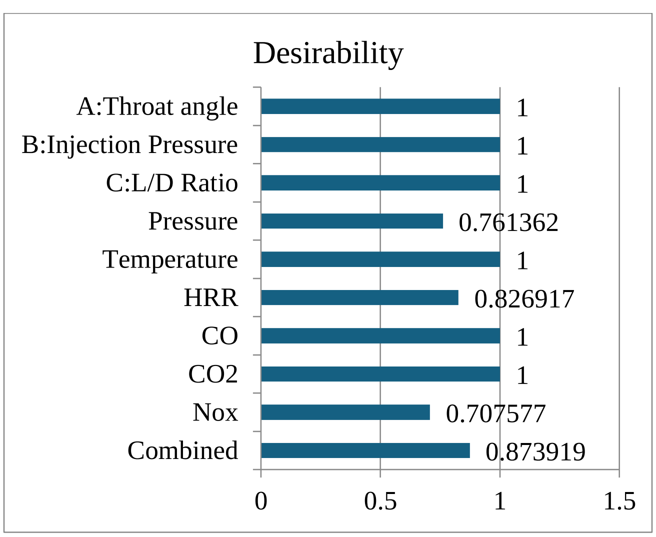

Fig. 14 Desirability for optimized values

The ramp plots for the optimal operating conditions and the accompanying responses are shown in Figure 13. The throat angle, injection pressure, and L/D ratio are each represented on a vertical panel at the top. The ramps' red dots show the ideal settings that have been chosen within each range. Here, the injection pressure is set at about 146 bar, the throat angle is fixed at 70°, and the L/D ratio is set at 2. The numbers were selected because they balance several answers at once and maximize the overall desirability function, which indicates the combined desirability as shown in Figure 14. The model predicts a pressure of about 65.1 bar, a temperature of 2693 K, an HRR of 244 J/CA, and emissions of 37.8 mg CO, 58.7 mg CO_2, and 0.097 mg NOx. The slope of each ramp shows whether the response increases or decreases with the factor settings. A rising ramp indicates a tendency toward higher response values at the selected optimum, while a declining ramp points to reduced response values.

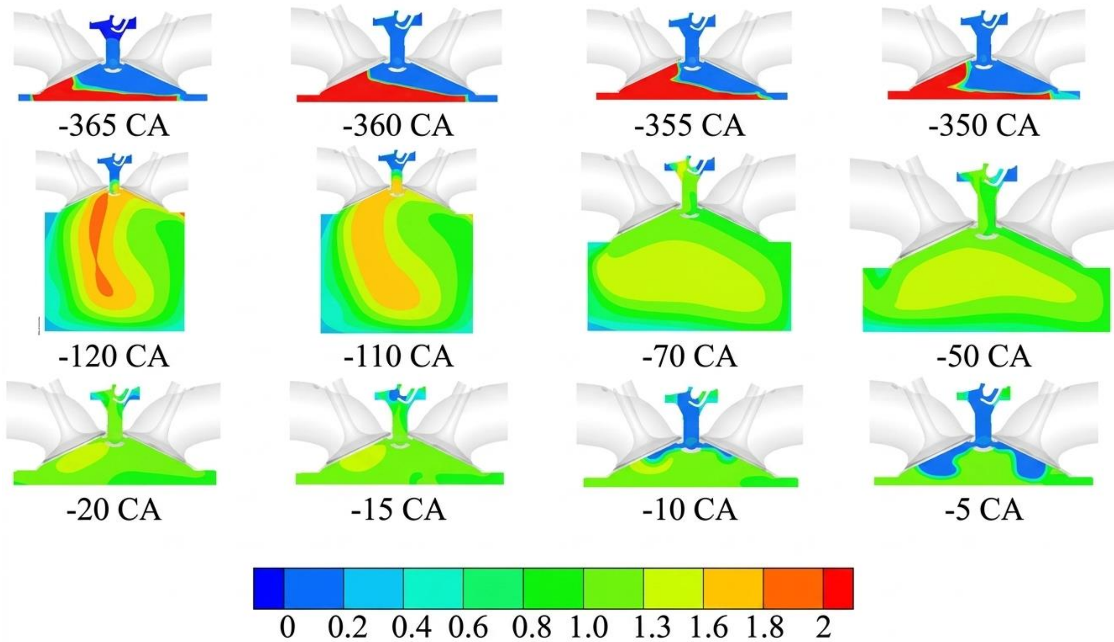

Fig. 15 Fuel-air equivalence ratio

Fuel-air equivalence ratio is a vital parameter that leads to better combustion to take place inside the cylinder. Figure 15 shows the fuel-air equivalence ratio for the crank angles from -365CA to -5CA. At -370 CA fuel is injected into the cylinder using an injector, and fuel spreads and mixes with the air gradually. The mixture ratio values were identified using the contours. The in-cylinder equivalence ratio distribution at different crank angle points is displayed in order to illustrate the temporal and spatial evolution of the fuel-air mixture during the intake and compression operations. Just after the intake valve opens, charge distribution is highly uneven at -365 CA. The initial fuel injection causes localized rich zones to form near the valve curtain region. As the crank angle increases to -360 CA and -355 CA, the mixing process grows, and the distribution spreads more in the cylinder. In the bulk volume, leaner areas are visible, but rich mixed pockets ($\phi > 1.6$) are seen close to the spray core. At -120 CA, we can able to observe that the fuel-air mixture occurs due to the tumble motion created inside, and further the mixing gets good and reaches to near stoichiometric around -20 CA, whereas some amount of rich mixture is found near the valve regions. This steady development emphasizes how important injection pressure, throat angle, and L/D ratio are for encouraging mixture preparation. Near ignition timing, a more uniform charge gradually replaces the various stratified mixture seen in the early crank angle phases. Such behavior promises an appropriate balance between combustion stability and flame propagation speed and affects the generation of emissions. Whereas later dilution with lean regions helps minimize the generation of CO and soot, early-phase rich regions promote ignition.

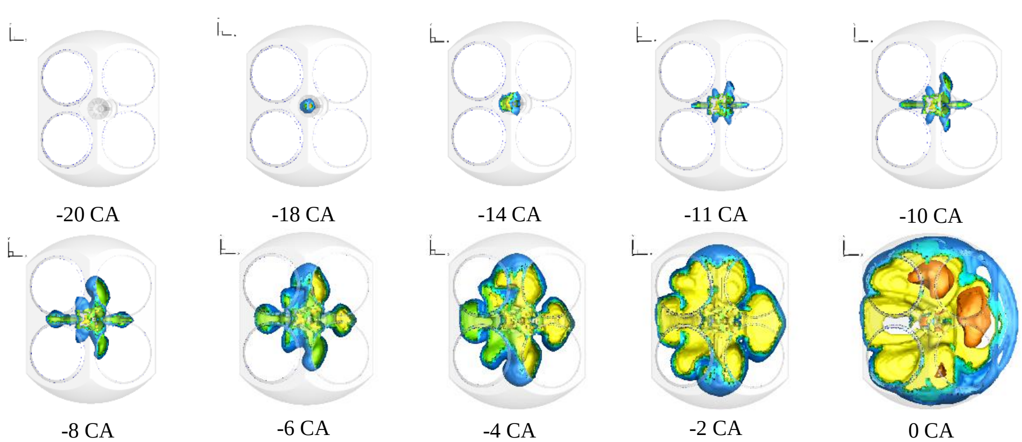

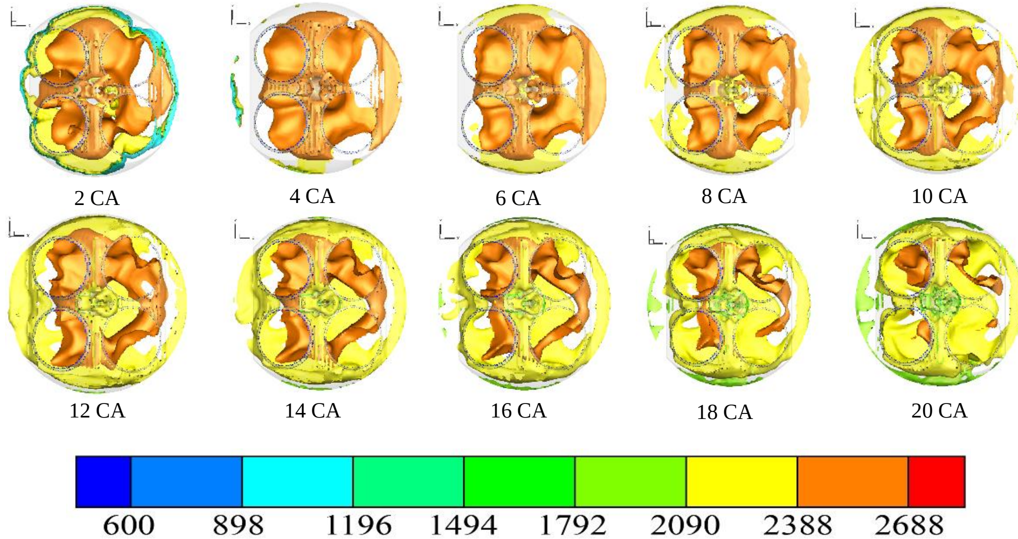

Fig. 16 Flame propagation from PCC to the main chamber

Burning development can be seen by in-cylinder temperature contours from -20 CA to +20 CA as shown in Figure 16. The chamber temperature stays uniformly compressed and rather low prior to TDC. When hot spots appear at TDC, ignition starts, and the temperature rises sharply as a result of the flames' quick spread. After ignition, maximum temperatures surpass 2600 K, yet the walls continue to have cooler areas because of heat transmission and quenching. The chamber is nearly completely burned by 20 CA, revealing a hot core encircled by cooler boundary layers. The in-cylinder thermodynamic evolution during the compression and combustion phases is clearly visualized by the series of temperature contour graphs from -20 CA to +20 CA. The temperature distribution is still fairly uniform at -20 CA, with lower values signifying compressed but unburned gases.

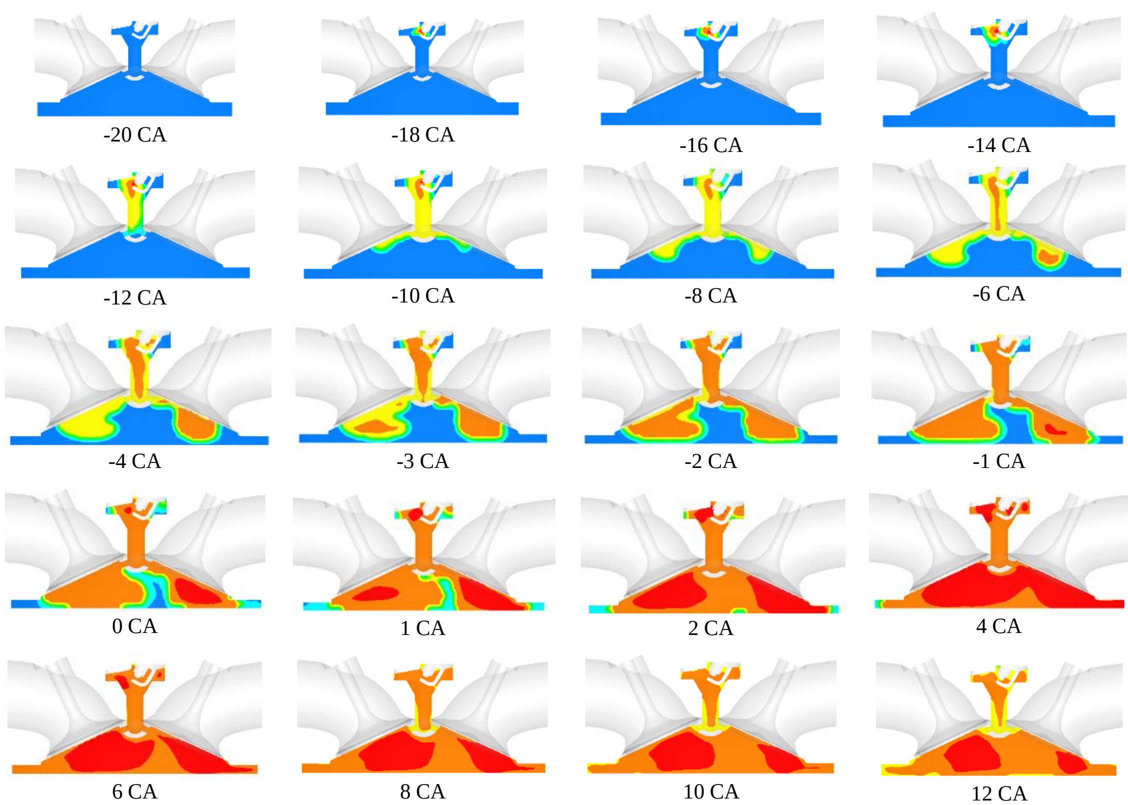

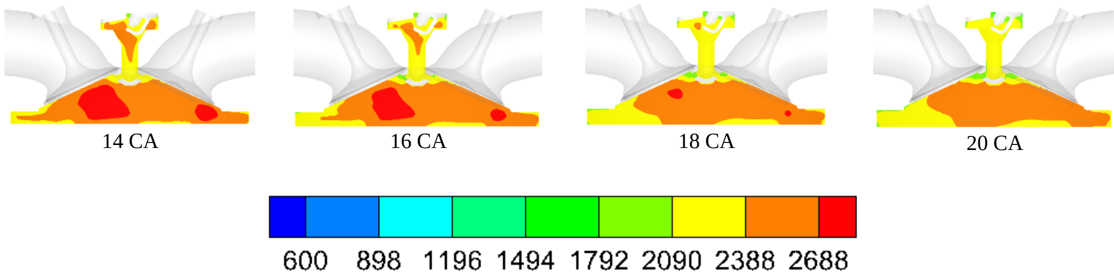

Fig. 17 Temperature distribution during the combustion process

The charge is still in the late compression stroke. Localized temperature increases in the spark ignition region occur as the piston approaches TDC, between -18 CA and -14 CA, indicating the start of pre-ignition heating. Early phases of combustion are indicated by the contours showing the initial shift from blue to green and yellow zones as the flame kernel starts to form between -12 CA and -10 CA. The flame spreads quickly across the combustion chamber at the next crank angles (-8 CA to -4 CA). Red and orange areas appear close to the ignition source and progressively expand outward, causing the temperature field to become extremely non-uniform. This phase represents the rapid heat release phase, when the temperature and pressure inside the cylinder are increased. When most of the charge is actively burning, the contours show the maximum flame development throughout the chamber at -3 CA to -1 CA. The highest temperatures, exceeding 2600 K in the core combustion region, occur at TDC (0 CA). The gas temperature starts to redistribute more evenly as the piston goes down after TDC (8 CA to 12 CA), but the central zones remain at high temperature. Figure 17 shows the temperature evolution in PCC and the main cylinder from -20 CA to +20 CA. The mixture present inside the PCC is ignited through the source at -20 CA. The flame travels through the pre-combustion chamber orifice into the main cylinder at 0 CA, where the remaining mixtures present inside the main cylinder are ignited using the rapid flame from the pre-combustion chamber. Flame velocity increases while it exits the orifice, which leads to the penetration of flame and also creates multiple ignition points inside the main cylinder.

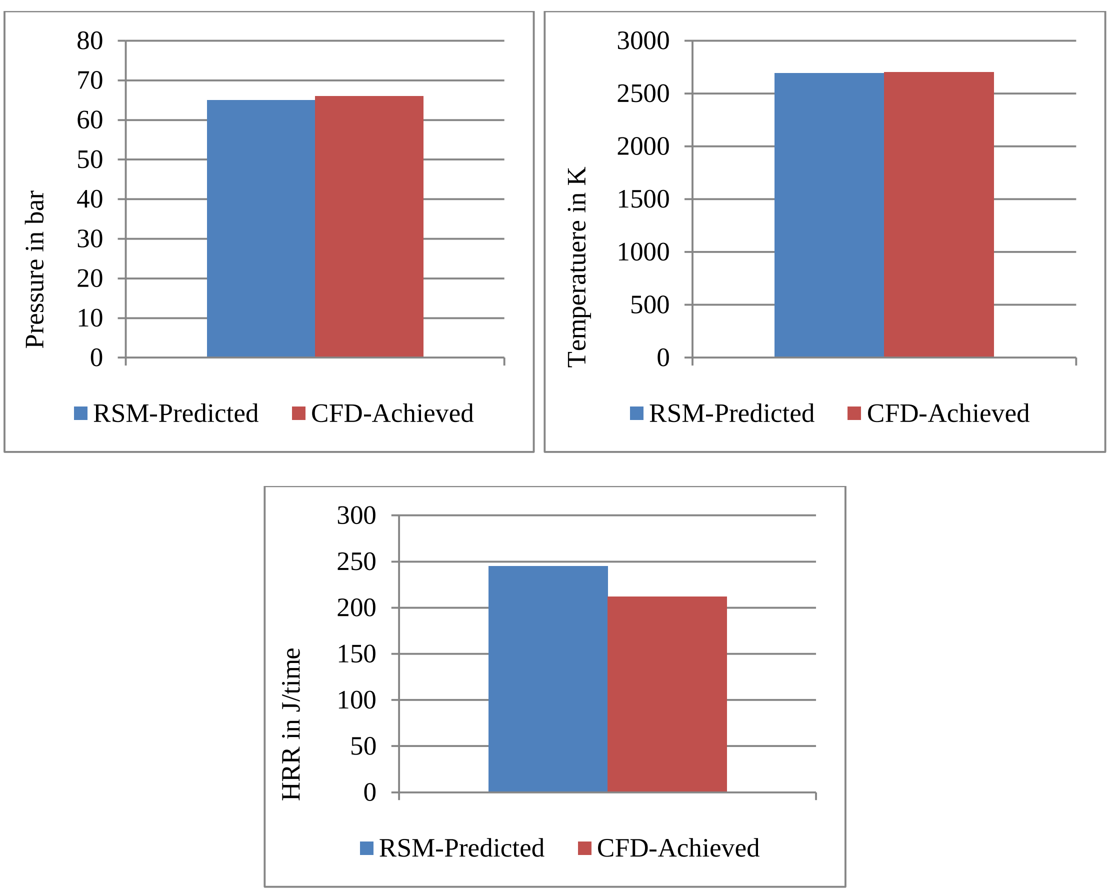

Fig. 18 Predicted vs. CFD chart for response pressure, temperature and HRR

The results of CFD simulations for temperature, pressure, and Heat Release Rate (HRR) are compared with outcomes predicted by the RSM model in Figure 18. There are only very small variations between the RSM-predicted pressure and temperature values and the CFD data, demonstrating the statistical model's durability in capturing combustion trends. When the CFD value is less than the RSM estimate, the HRR demonstrates a somewhat wider gap between simulation and prediction. The variation can result from the fact that RSM predictions are based on fitting mathematical relationships, whereas CFD captures detailed in-cylinder flow and combustion dynamics.

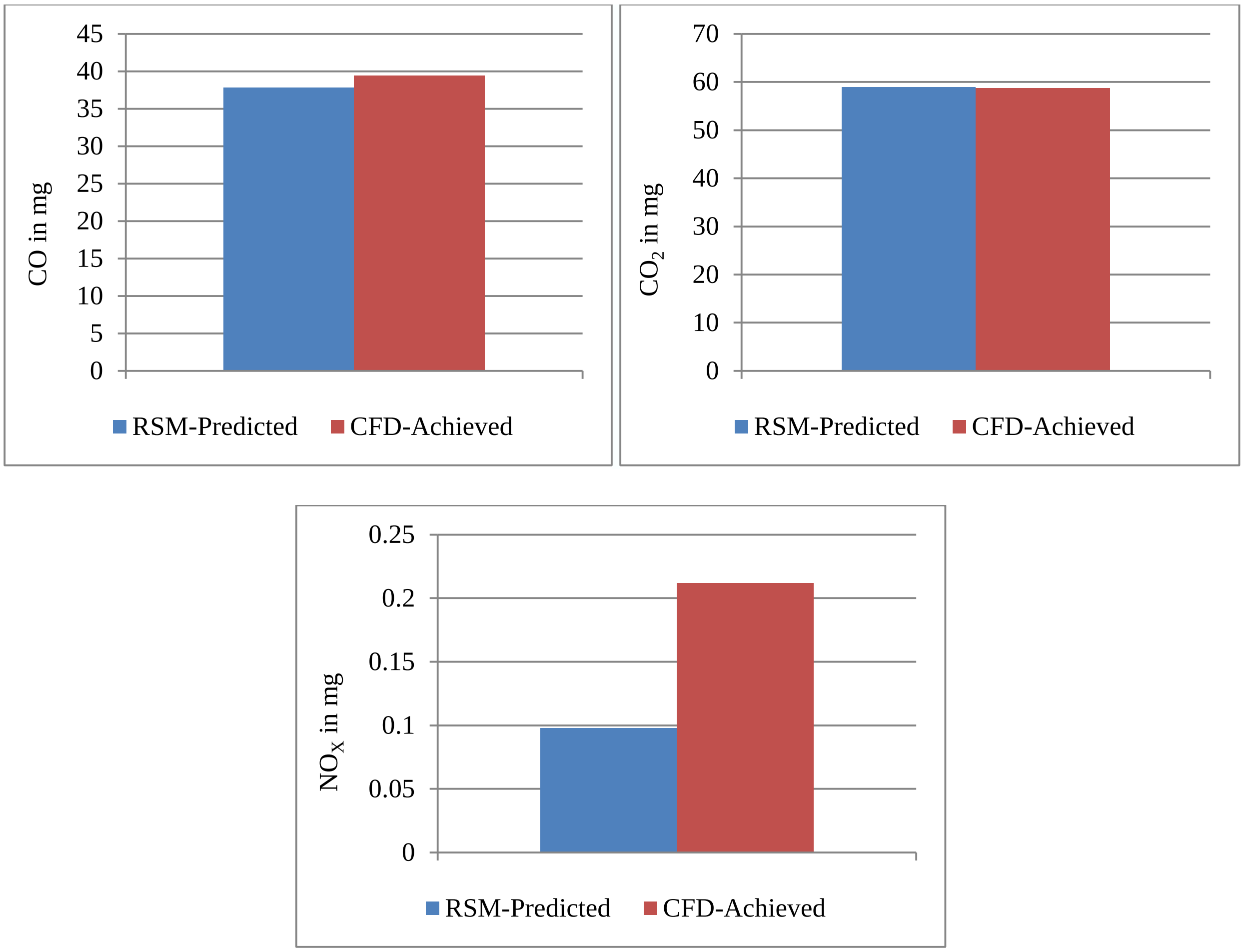

Fig. 19 Predicted vs. CFD chart for response CO, CO_2, and NO_X

Figure 19 compares predictions and actual values for CO, CO_2, and NO_x made by two different methods: the Response Surface Methodology (RSM) and Computational Fluid Dynamics (CFD). The outcomes for CO and CO_2 were very similar. The statistical model appears to be quite effective for these two outputs, as the RSM model predicted values that were nearly identical to what the CFD analysis obtained. However, for NO_x, conditions were different. The value obtained using CFD was twice that of the RSM model. This significant difference suggests that although model prediction is good for responses CO and CO_2, even though prediction was not good for the response NO_x.

4. Conclusion

The validation between the RSM predictions and CFD results shows that most of the parameters were predicted accurately. The differences for pressure, 1.93%, and temperature, 0.25%, indicate that the in-cylinder behavior is predicted properly. The values for CO and CO_2 are 3% and 0.03%, respectively, indicating that the quadratic model is good in order to predict general emission levels. The higher variation is achieved for responses such as heat release rate (13%) and especially for NOx (53%). This happened because RSM is not able to predict the localized effects. Through CFD simulations coupled with Response Surface Methodology (RSM), the influence of factors such as orifice angle, injection pressure, and L/D ratio and their interaction effect on responses was observed. RSM predictions for performance parameters such as pressure, temperature, and heat release rate are monitored. While validating the RSM predicted values with CFD achieved values, responses pressure and temperature were attained accurately as per the predictions from RSM, while the heat release rate shows a slight drop when compared with CFD responses, and this happens because of the factors' influence on the response parameters. Similarly, for emission parameters, CO and CO_2 predictions were accurate when compared to the response NO_x. This occurs due to the limitation of the RSM quadratic model when compared to CFD. The simulation predicts high temperature local zones more accurately what RSM lacks.

Conflicts of Interest

The author(s) declare(s) that there is no conflict of interest regarding the publication of this paper.

References

[1] Shweta Singh et al., "An Overview of Vehicular Emission Standards," *MAPAN*, vol. 38, pp. 241-263, 2023. [CrossRef] [Google Scholar] [Publisher Link]

[2] Madhur D. Gajbhiye et al., "Evolution and Mitigation of Vehicular Emissions Due to India's Bharat Stage Emission Standards – A Case Study from Delhi," *Environmental Development*, vol. 45, 2023. [CrossRef] [Google Scholar] [Publisher Link]

[3] Revati Borkhade et al., "Implementation of Sustainable Reforms in the Indian Automotive Industry: From Vehicle Emissions Perspective," *Cogent Engineering*, vol. 9, no. 1, pp. 1-15, 2022. [CrossRef] [Google Scholar] [Publisher Link]

[4] Ahmed A. Alharbi, "An Investigation of Nox Emissions and Fuel Consumption from SI Engines Using Blends of Gasoline, Hydrogen-Rich Synthesis Gas, and Hydrous Ethanol," *Proceedings of the 9th World Congress on Civil, Structural, and Environmental Engineering (CSEE 2024*, London, United Kingdom, pp. 1-2, 2024. [Google Scholar] [Publisher Link]

[5] Srinivasa Krishna Addepalli, and J. M. Mallikarjuna, *Modelling Spray in GDI Engines: Fuel Injection Modelling*, Modelling Spark Ignition Combustion, Springer Singapores, pp. 339-389, 2024. [CrossRef] [Google Scholar] [Publisher Link]

[6] Soo-Jin Jeong, "CFD Simulation of Pre-Chamber Spark-Ignition Engines—A Perspective Review," *Energies*, vol. 17, no. 18, pp. 1-39, 2024. [CrossRef] [Google Scholar] [Publisher Link]

[7] Haiwen Ge et al., "CFD Optimization of the Pre-Chamber Geometry for a Gasoline Spark Ignition Engine," *Frontiers in Mechanical Engineering*, vol. 6, pp. 1-18, 2020. [CrossRef] [Google Scholar] [Publisher Link]

[8] R. Novella et al., "Effects of Pre-Chamber Flow-Field on Combustion Stability in a Spark-Ignition Engine using Large-Eddy Simulations," *Physics of Fluids*, vol. 35, no. 11, 2023. [CrossRef] [Google Scholar] [Publisher Link]

[9] Mickael Silva et al., "Computational Assessment of Effects of Throat Diameter on Combustion and Turbulence Characteristics in a Pre-Chamber Engine," *Applied Thermal Engineering*, vol. 212, 2022. [CrossRef] [Google Scholar] [Publisher Link]

[10] Xinlei Liu et al., "Computational Assessment of the Effects of Pre-Chamber and Piston Geometries on the Combustion Characteristics of an Optical Pre-Chamber Engine," *Fuel*, vol. 341, 2023. [CrossRef] [Google Scholar] [Publisher Link]

[11] A. Piano et al., "CFD-Based Methodology for the Characterization of the Combustion Process of a Passive Pre-Chamber Gasoline Engine," *Transportation Engineering*, vol. 13, pp. 1-13, 2023. [CrossRef] [Google Scholar] [Publisher Link]

[12] Josip Krajnović et al., "A Novel Concept of Active Pre-Chamber Engine with a Single Injector – The Passive Main Chamber Approach," *Applied Thermal Engineering*, vol. 250, 2024. [CrossRef] [Google Scholar] [Publisher Link]

[13] Viktor Dilber et al., "Optimization of Pre-Chamber Geometry and Operating Parameters in a Turbulent Jet Ignition Engine," *Energies*, vol. 15, no. 13, pp. 1-21, 2022. [CrossRef] [Google Scholar] [Publisher Link]

[14] Simone Bigalli et al., "Numerical Investigation on the Performance of a 4-Stroke Engine with Different Passive Pre-Chamber Geometries Using a Detailed Chemistry Solver," *Energies*, vol. 15, no. 14, pp. 1-18, 2022. [CrossRef] [Google Scholar] [Publisher Link]

[15] Paolo Sementa et al., "Custom-Designed Pre-Chamber: Investigating the Effects on Small SI Engine in Active and Passive Modes," *Energies*, vol. 16, no. 13, pp. 1-24, 2023. [CrossRef] [Google Scholar] [Publisher Link]

[16] Federico Millo et al., "Experimental and Numerical Investigation of a Passive Pre-Chamber Jet Ignition Single-Cylinder Engine," *SAE International 15th International Conference on Engines & Vehicles*, Capri, Italy, 2021. [CrossRef] [Google Scholar] [Publisher Link]

[17] Emmanuele Frasci et al., "Impact of Prechamber Design and Air–Fuel Ratio on Combustion and Fuel Consumption in a SI Engine Equipped with a Passive TJI," *Fuel*, vol. 345, pp. 1-14, 2023. [CrossRef] [Google Scholar] [Publisher Link]

[18] Mohan Raj Peethambaram et al., "Combustion Analysis of Active Pre-Chamber Design for Ultra-Lean Engine Operation," *SAE International Journal of Engines*, vol. 17, no. 5, pp. 705-720, 2024. [CrossRef] [Google Scholar] [Publisher Link]

[19] Hailiang Kou et al., "General Comparison of Pre-Chamber Jet Ignition and Spark Ignition on Combustion and Emission Characteristics of a Methanol Direct Injection Engine," *Case Studies in Thermal Engineering*, vol. 70, pp. 1-16, 2025. [CrossRef] [Google Scholar] [Publisher Link]

[20] Ponnya Hlaing et al., "Estimates of the Air-Fuel Ratio at the Time of Ignition in a Pre-Chamber using a Narrow throat Geometry," *International Journal of Engine Research*, vol. 24, no. 2, pp. 622-638, 2023. [CrossRef] [Google Scholar] [Publisher Link]

[21] Linhui Huang et al., "A New Design Criterion for Narrow Throat Pre-Chamber to Achieve High Jet and Ignition Performance," *Applied Thermal Engineering*, vol. 258, 2025. [CrossRef] [Google Scholar] [Publisher Link]

[22] Jingxun Yang et al., "Influence of Structure Parameters of Pre-Chamber on Lean Combustion of Active Pre-Chamber Jet Ignition Engine," *Energy*, vol. 304, 2024. [CrossRef] [Google Scholar] [Publisher Link]

[23] Ponnya Hlaing et al., "Effects of Volume and Nozzle Area in Narrow-Throat Spark-Ignited Pre-Chamber Combustion Engines," *Fuel*, vol. 313, pp. 1-37, 2022. [CrossRef] [Google Scholar] [Publisher Link]
[24] Priybrat Sharma et al., "Optical Study of Active Narrow Throat Pre-Chamber Assisted Internal Combustion Engine at Lean Limit," *Applications in Energy and Combustion Science*, vol. 16, pp. 1-14, 2023. [CrossRef] [Google Scholar] [Publisher Link]
[25] Rudolf Tomić et al., "Influence of Pre-Chamber Volume, Orifice Diameter and Orifice Number on Performance of Pre-Chamber SI Engine—An Experimental and Numerical Study," *Energies*, vol. 16, no. 6, pp. 1-9, 2023. [CrossRef] [Google Scholar] [Publisher Link]
[26] Paresh D. Patel, Absar Lakdawala, and Rajesh N. Patel, "Box–Behnken Response Surface Methodology for Optimization of Operational Parameters of Compression Ignition Engine Fuelled with a Blend of Diesel, Biodiesel and Diethyl Ether," *Biofuels*, vol. 7, no. 2, pp. 87-95, 2016. [CrossRef] [Google Scholar] [Publisher Link]
[27] Sathiyamoorthi Ramalingam et al., "Analysis of Optimising Injection Parameters and EGR for DICI Engine Performance Powered by Lemongrass Oil using Box–Behnken (RSM) Modelling," *International Journal of Ambient Energy*, vol. 43, no. 1, pp. 6362-6379, 2022. [CrossRef] [Google Scholar] [Publisher Link]
[28] Siva Prasad Kattela, Srinivasa Rao Surapaneni, and Raju V. R. K, "Parametric Optimization of a Direct Injection - Compression Ignition Engine Fuelled with Butanol/Diesel Blend using Response Surface Methodology," *Environmental Progress & Sustainable Energy*, vol. 39, no. 3, 2020. [CrossRef] [Google Scholar] [Publisher Link]
[29] Prabhakara Rao Ganji et al., "Optimisation of EGR and SOI for Better Combustion Characteristics using Response Surface Methodology," *International Journal of Ambient Energy*, vol. 42, no. 14, pp. 1660-1669, 2021. [CrossRef] [Google Scholar] [Publisher Link]
[30] Bin Zheng et al., "Optimization of Engine Piston Performance Based on Multi-Method Coupling: Sensitivity Analysis, Response Surface Model, and Application of Genetic Algorithm," *Materials*, vol. 18, no. 13, pp. 1-24, 2025. [CrossRef] [Google Scholar] [Publisher Link]
[31] Nalini Kanta Mukherjee et al., "Optimization of a 3D Combustion Bowl Geometry Using Response Surface Modeling," *SAE International Journal of Engines*, vol. 14, no. 2, pp. 173-198, 2021, 2025. [CrossRef] [Google Scholar] [Publisher Link]
[32] Sipeng Zhu et al., "A Review of the Pre-Chamber Ignition System Applied on Future Low-Carbon Spark Ignition Engines," *Renewable and Sustainable Energy Reviews*, vol. 154, 2022. [CrossRef] [Google Scholar] [Publisher Link]
[33] Štěpán Kyjovský et al., "Experimental Investigation on Pre-Chamber Geometry for Passenger Car Engine," *Energy Conversion and Management*, vol. 352, 2026. [CrossRef] [Google Scholar] [Publisher Link]
[34] Leng Xianyin et al., "Impact of the Pre-Chamber Nozzle Orifice Configurations on Combustion and Performance of a Natural Gas Engine," *Thermal Science*, vol. 22, no. 3, pp. 1325-1337, 2018. [CrossRef] [Google Scholar] [Publisher Link]
[35] Lei Zhou et al., "Effects of Different Hole Structures of Pre-Chamber with Turbulent Jet Ignition on the Flame Propagation and Lean Combustion Performance of a Single-Cylinder Engine," *Fuel*, vol. 308, 2022. [CrossRef] [Google Scholar] [Publisher Link]
[36] Akichika Yamaguchi et al., "Spray Behaviors and Gasoline Direct Injection Engine Performance Using Ultrahigh Injection Pressures up to 1500 Bar," *SAE International Journal of Engines*, vol. 15, no. 2, pp. 167-183, 2022. [CrossRef] [Google Scholar] [Publisher Link]
[37] L. F. Gutiérrez, Jose P. Tamagno, and Sergio A. Elaskar, "RANS Simulation of Turbulent Diffusive Combustion using Open Foam," *Journal of Applied Fluid Mechanics*, vol. 9, no. 2, pp. 669-682, 2016. [Google Scholar] [Publisher Link]
[38] Stefan Posch et al., "Finding the Optimum Design of Large Gas Engines Prechambers Using CFD and Bayesian Optimization," *arXiv preprint*, pp. 1-9, 2023. [CrossRef] [Google Scholar] [Publisher Link]
[39] Lorenzo Piu et al., "A Data-Driven Approach to Refine the Partially Stirred Reactor Closure for Turbulent Premixed Flames," *Flow Turbulence Combust*, vol. 115, pp. 1235-1260, 2025. [CrossRef] [Google Scholar] [Publisher Link]
[40] Srabani Podder, and Sudipta Mukherjee, "Response Surface Methodology (RSM) as a Tool in Pharmaceutical Formulation Development," *Asian Journal of Pharmaceutical and Clinical Research*, vol. 17, no. 11, pp. 18-25, 2024. [CrossRef] [Google Scholar] [Publisher Link]
[41] Dharmaraja Selvamuthu, and Dipayan Das, *Response Surface Methodology*, Introduction to Probability, Statistical Methods, Design of Experiments and Statistical Quality Control, Springer, pp. 493-525, 2024. [CrossRef] [Google Scholar] [Publisher Link]
[42] D. Raghavarao, and S. Altan, "Response Surface Methodology," *Wiley Encyclopedia of Clinical Trials*, 2008. [CrossRef] [Google Scholar] [Publisher Link]
[43] Sathish Thanikodi, Saravanan Rathinasamy, and Jothi Arunachalam Solairaju, "Developing a Model to Predict and Optimize the Flexural and Impact Properties of Jute/Kenaf Fiber Nano-composite using Response Surface Methodology," *The International Journal of Advanced Manufacturing Technology*, vol. 136, pp. 195-209, 2025. [CrossRef] [Google Scholar] [Publisher Link]
[44] S. L. C. Ferreira et al., "Box-Behnken Design: An Alternative for the Optimization of Analytical Methods," *Analytica Chimica Acta*, vol. 597, no. 2, pp. 179-186, 2007. [CrossRef] [Google Scholar] [Publisher Link]